
Implicit-explicit schemes for compressible Cahn-Hilliard-Navier-Stokes equations

Pep Mulet

the date of receipt and acceptance should be inserted later

Abstract The isentropic compressible Cahn-Hilliard-Navier-Stokes equations is a system of fourth-order partial differential equations that model the evolution of some binary fluids under convection.

The purpose of this paper is the design of efficient numerical schemes to approximate the solution of initial-boundary value problems with these equations. The efficiency stems from the implicit treatment of the high-order terms in the equations. Our proposal is a second-order linearly implicit-explicit time stepping scheme applied in a method of lines approach, in which the convective terms are treated explicitly and only linear systems have to be solved.

Some experiments are performed to assess the validity and efficiency of this proposal.

Keywords Cahn-Hilliard equation, Navier-Stokes equations, implicit-explicit schemes.

1 Introduction

According to Kynch's theory (see [11]) for sedimentation of homogeneous monodisperse suspensions, consisting of solid spherical particles of the same diameter and density immersed in a viscous fluid, two interfaces form in the settling process: a descending interface between the clear liquid and the initial homogeneous mixture and an ascending interface between the maximally concentrated mixture and the initial homogeneous mixture.

In [16], it is observed that, after several days, a colloidal monodisperse suspension of polystyrene particles sediments forming a layered structure a fact that contradicts Kynch's theory. A spinodal decomposition, governed by the Cahn-Hilliard equation [6], is then conjectured as the underlying mechanism that explains this phenomenon.

The Cahn-Hilliard equation cannot explain, by itself, this layering phenomenon, for it does not take into account the gravitational force. This may be introduced

into the model by means of conservation of individual species and bulk momenta. Ignoring temperature, this yields a system of equations, the isentropic Cahn-Hilliard-Navier-Stokes equations [12, 1], which are a system of fourth-order partial differential equations that model the evolution of mixtures of binary fluids under convective effects.

Although (quasi) incompressible versions of these equations might be more suitable for explaining the cited layering phenomenon, we consider the compressible case for the evolution of, e.g. foams, solidification processes, fluid-gas interface.

This paper aims to propose numerical methods that use implicit-explicit time-stepping schemes to avoid the severe restriction posed by the fourth-order terms for the efficient numerical solution of boundary-initial problems with these equations.

The paper is organized as follows: in section 2 the compressible isentropic Cahn-Hilliard-Navier-Stokes equations are introduced; in section 3 implicit-explicit Runge-Kutta numerical schemes for the two-dimensional equations are proposed; in section 4 we perform some numerical experiments to assess the efficiency of our proposals; finally, in section 5 we draw some conclusions and give some perspectives for future research.

2 Cahn-Hilliard-Navier-Stokes equations

The models in this exposition are based on [1]. We denote by c_i , the mass concentration of species $i = 1, 2$, by $c = c_1 - c_2$, by ρ the density of the mixture and by \mathbf{v} its bulk velocity (we use boldface for vector variables).

We denote by Ω the open set in \mathbb{R}^3 that is filled by the fluids and by ε a parameter related to the thickness of the diffuse interface of the fluid mixture. The Ginzburg-Landau free energy in some region $V \subseteq \Omega$ of the immiscible compressible two-phase fluid is

$$\begin{aligned} E(\rho, c) &= \int_V (\rho f(\rho, c) + \frac{\varepsilon}{2} |\nabla c|^2) dx \\ f(\rho, c) &= f_e(\rho) + \psi(c) \end{aligned}$$

where $\psi(c) = \frac{1}{4}(c^2 - 1)^2$ is a double-well potential function and f_e is the specific Helmholtz free energy of an equivalent one-phase fluid.

The isentropic compressible Cahn-Hilliard-Navier-Stokes equations with gravitation are the following equations:

$$\begin{cases} \rho_t + \operatorname{div}(\rho \mathbf{v}) = 0, \\ (\rho \mathbf{v})_t + \operatorname{div}(\rho \mathbf{v} \otimes \mathbf{v}) = \rho \mathbf{G} + \operatorname{div} \mathbb{T}, \\ (\rho c)_t + \operatorname{div}(\rho c \mathbf{v}) = \Delta \mu, \end{cases} \quad (1)$$

where div is the divergence operator with respect to $x \in \mathbb{R}^3$, the first equation is the continuity equation for the mixture, the second is the equation for conservation of bulk momenta. In these equations

$$\mathbb{T} = \nu(c)(\nabla \mathbf{v} + \nabla \mathbf{v}^T) + (\lambda(c) \operatorname{div} \mathbf{v} - p(\rho, c))\mathbb{I} + \frac{\varepsilon}{2} |\nabla c|^2 \mathbb{I} - \varepsilon (\nabla c \otimes \nabla c)$$

is the stress tensor, $p(\rho, c) = \rho^2 \frac{\partial f(\rho, c)}{\partial \rho}$ is the fluid pressure, $\nu(c), \lambda(c) > 0$ are the viscosity coefficients, \mathbf{G} is the gravitational acceleration, and

$$\mu = \psi'(c) - \frac{\varepsilon}{\rho} \Delta c,$$

is the chemical potential.

The $(\rho, \rho \mathbf{v})$ -subsystem, with $\varepsilon = 0$, form the compressible isentropic Navier-Stokes equations. The equation for ρc , for constant ρ (which may be assumed to be 1) and $\mathbf{v} = 0$, is the Cahn-Hilliard equation [6].

$$c_t = \Delta(\psi'(c) - \varepsilon \Delta c). \quad (2)$$

These equations are supplemented by initial conditions $\rho_0, \mathbf{v}_0, c_0$ and the boundary conditions

$$\mathbf{v}|_{\partial\Omega} = \nabla c \cdot \mathbf{n}|_{\partial\Omega} = \nabla \mu \cdot \mathbf{n}|_{\partial\Omega} = 0, \quad (3)$$

where \mathbf{n} is the outward normal vector to the boundary.

In [1] it is proved that these equations admit weak solutions, with renormalization of ρ in the sense of Di Perna and Lions, in any interval $[0, T], T > 0$, provided $\gamma > \frac{3}{2}$, $0 \leq \rho_0 \in L^\gamma(\Omega), \rho_0 |v_0|^2 \in L^1(\Omega), c_0 \in H^1(\Omega)$.

We henceforth consider $\nu(c), \lambda(c)$ constant and $p = p(\rho) = \rho^\gamma$, for the adiabatic constant $\gamma > 1.5$, which corresponds to $f_\varepsilon(\rho) = \frac{\rho^{\gamma-1}}{\gamma-1}$. Therefore, the equation for the conservation of bulk momenta can be rewritten as:

$$\begin{aligned} (\rho \mathbf{v})_t + \operatorname{div}(\rho \mathbf{v} \otimes \mathbf{v} + p(\rho) \mathbb{I}) \\ = \rho \mathbf{G} + (\nu + \lambda) \nabla \operatorname{div} \mathbf{v} + \nu \Delta \mathbf{v} + \frac{\varepsilon}{2} \nabla |\nabla c|^2 - \varepsilon \operatorname{div}(\nabla c \otimes \nabla c). \end{aligned}$$

As expected, the ρ and $q = \rho c$ variables are conserved since the respective associated fluxes,

$$\rho \mathbf{v} \cdot \mathbf{n}, \quad (q \mathbf{v} - \nabla \mu) \cdot \mathbf{n},$$

vanish at the boundary due to (3).

The two-dimensional version of these equations, for $\mathbf{v} = (v_1, v_2)$, is:

$$\begin{aligned} \rho_t + (\rho v_1)_x + (\rho v_2)_y &= 0, \\ (\rho v_1)_t + (\rho v_1^2 + \rho^\gamma)_x + (\rho v_1 v_2)_y &= \frac{\varepsilon}{2} (c_y^2 - c_x^2)_x - \varepsilon (c_x c_y)_y \\ &\quad + \nu \Delta v_1 + (\nu + \lambda) ((v_1)_{xx} + (v_2)_{xy}), \\ (\rho v_2)_t + (\rho v_1 v_2)_x + (\rho v_2^2 + \rho^\gamma)_y &= \rho G + \frac{\varepsilon}{2} (c_x^2 - c_y^2)_y - \varepsilon (c_x c_y)_x \\ &\quad + \nu \Delta v_2 + (\nu + \lambda) ((v_1)_{xy} + (v_2)_{yy}), \\ (\rho c)_t + (\rho c v_1)_x + (\rho c v_2)_y &= \Delta(\psi'(c) - \frac{\varepsilon}{\rho} \Delta c), \end{aligned} \quad (4)$$

where $\Delta w = w_{xx} + w_{yy}$ and gravity acts along the y coordinate.

We also consider the one-dimensional version of these equations:

$$\begin{aligned}\rho_t + (\rho v)_x &= 0, \\ (\rho v)_t + (\rho v^2 + p(\rho))_x &= \rho G + \left((2\nu + \lambda)v_x - \frac{\varepsilon}{2}c_x^2 \right)_x, \\ (\rho c)_t + (\rho cv)_x &= (\psi'(c) - \frac{\varepsilon}{\rho}c_{xx})_{xx},\end{aligned}\tag{5}$$

where gravity acts along the x coordinate.

2.1 Spinodal decomposition

The Cahn-Hilliard equation was proposed in [6] (see also [7]) to model the separation of a homogeneous mixture of two incompressible fluids, the first of them stable with respect to the presence of small quantities of the second one, and this one unstable with respect to the presence of small quantities of the first one. The boundary of the unstable region in (c, T, p) -space, T, p being temperature and pressure, respectively, is given by the equation $\frac{\partial^2 G}{\partial c^2} = 0$, where $G(c, T, p)$ is the Gibbs free energy density of the fluid, and is usually named the spinodal.

To analyze the spinodal decomposition, we consider the linearization of (2) about a constant state c_0 in the spinodal region $(-\frac{1}{\sqrt{3}}, \frac{1}{\sqrt{3}})$, i.e., $\psi''(c_0) < 0$:

$$c(x, t) = c_0 + u(x, t),$$

for assumedly small u , with $\int_{\Omega} u = 0$. Notice then that $\psi'(c_0 + u(x, t)) = \psi'(c_0) + \psi''(c_0)u(x, t) + \mathcal{O}(u^2)$, therefore the linearized Cahn-Hilliard equation:

$$u_t = \psi''(c_0)\Delta u - \varepsilon\Delta^2 u.\tag{6}$$

is deduced from the Cahn-Hilliard equation (2).

By separation of variables, functions of the form

$$u(x, t) = v(t) \prod_{i=1}^3 \cos(k_i \pi x_i), \quad k_i \in \mathbb{N},\tag{7}$$

satisfy the homogeneous Neumann boundary conditions and $\int_{\Omega} u(x, t) dx = 0$, and are, therefore, solutions of (6) if

$$v'(t) = \left(-\psi''(c_0) \sum_i k_i^2 \pi^2 - \varepsilon (\sum_i k_i^2 \pi^2)^2 \right) v(t),$$

which yield solutions

$$v(t) = v(0) e^{-\left(\psi''(c_0) \sum_i k_i^2 \pi^2 + \varepsilon (\sum_i k_i^2 \pi^2)^2 \right) t}.\tag{8}$$

The linearized equation (2) will therefore develop instabilities provided

$$\psi''(c_0) \sum_i k_i^2 \pi^2 + \varepsilon (\sum_i k_i^2 \pi^2)^2 < 0,$$

for some $k_i \geq 1$, and this will be so if $\varepsilon\pi^2 + \psi''(c_0) < 0$. But these instabilities, triggered by the linearized equation, will grow until some point, when the nonlinear character of the Cahn-Hilliard equations makes the linearization no longer valid, and will stop, since energy decreases with time as shown here:

$$\begin{aligned} \frac{d}{dt}F(c(\cdot, t)) &= \int_{\Omega} (\psi'(c)c_t + \varepsilon\nabla c \nabla c_t) dx = \int_{\Omega} (\psi'(c)c_t - \varepsilon\Delta c c_t) dx + \int_{\partial\Omega} \varepsilon c_t \nabla c \cdot \mathbf{n} dx \\ &= - \int_{\Omega} (\psi'(c) - \varepsilon\Delta c)^2 dx \leq 0, \end{aligned}$$

by using differentiation under the integral, integration by parts and the Neumann boundary conditions for c .

3 Numerical schemes

Numerical schemes for the Cahn-Hilliard equation can be found, e.g., in [8, 7], and, for the quasi-incompressible Cahn-Hilliard-Navier-Stokes, in, e.g., [10, 19, 14]. In [9] there is a numerical study for compressible Cahn-Hilliard-Navier-Stokes that mainly focus on the convective part.

Our purpose is to design finite differences numerical methods for the efficient approximate solution of the two-dimensional equations in Section 2. For this, we consider $\Omega = (0, 1)^2$ and the equispaced computational grid given by the M^2 nodes $x_{i,j} = ((i - \frac{1}{2})h, (j - \frac{1}{2})h)$, $i, j = 1, \dots, M$, where $h = \frac{1}{M}$ and denote by (x, y) the spatial variable.

We denote by

$$u = (\rho, \mathbf{m}, q), \mathbf{m} = (m_1, m_2) = (\rho v_1, \rho v_2) = \rho \mathbf{v}, q = \rho c,$$

the vector of conserved variables and aim to approximate (4) by a spatial semi-discretization consisting of $4M^2$ ordinary differential equations

$$u'_{k,i,j}(t) = \mathcal{L}(U(t))_{k,i,j}, k = 1, \dots, 4, i, j = 1, \dots, M,$$

for $4M^2$ unknowns $u_{k,i,j}(t) \in \mathbb{R}^4$ which are approximations of $u_k(x_{i,j}, t)$ and form the $4M^2$ (column) vector function $U(t)$ by using lexicographical order so that

$$U = \begin{bmatrix} \varrho \\ \varrho * V_1 \\ \varrho * V_2 \\ \varrho * C \end{bmatrix}, \quad (\varrho * S)_i = \varrho_i S_i,$$

$$\rho(x_{i,j}, t) \approx \varrho_{M(i-1)+j}(t),$$

$$v_k(x_{i,j}, t) \approx (V_k)_{M(i-1)+j}(t), k = 1, 2,$$

$$c(x_{i,j}, t) \approx C_{M(i-1)+j}(t).$$

For the sake of notation and simplicity we seamlessly use a slight abuse of notation when identifying, e.g., $\varrho_{i,j} \equiv \varrho_{M(i-1)+j}$. We also use superindices for M^2 block notation, e.g., $U^1 = \varrho$.

The nonzero terms in the spatial semidiscretization

$$\mathcal{L}(U) = \mathcal{C}(U) + \mathcal{L}_1(U) + \mathcal{L}_2(U) + \mathcal{L}_3(U) + \mathcal{L}_4(U) \quad (9)$$

are the following:

$$\begin{aligned}
\mathcal{C}(U)_{1,i,j} &\approx -((\rho v_1)_x + (\rho v_2)_y)(x_{i,j}, t), \\
\mathcal{C}(U)_{2,i,j} &\approx -((\rho v_1^2 + \rho^\gamma)_x + (\rho v_1 v_2)_y)(x_{i,j}, t), \\
\mathcal{C}(U)_{3,i,j} &\approx -((\rho v_1 v_2)_x + (\rho v_2^2 + \rho^\gamma)_y)(x_{i,j}, t), \\
\mathcal{C}(U)_{4,i,j} &\approx -((\rho c v_1)_x + (\rho c v_2)_y)(x_{i,j}, t), \\
\mathcal{L}_1(U)_{3,i,j} &= \rho_{i,j} G \approx \rho(x_{i,j}, t) G, \\
\mathcal{L}_2(U)_{2,i,j} &\approx \varepsilon \left(\frac{1}{2} (c_y^2)_x - \frac{1}{2} (c_x^2)_x - (c_x c_y)_y \right) (x_{i,j}, t), \\
\mathcal{L}_2(U)_{3,i,j} &\approx \varepsilon \left(\frac{1}{2} (c_x^2)_y - \frac{1}{2} (c_y^2)_y - (c_x c_y)_x \right) (x_{i,j}, t), \\
\mathcal{L}_3(U)_{4,i,j} &\approx \Delta(\psi'(c) - \frac{\varepsilon}{\rho} \Delta c)(x_{i,j}, t), \\
\mathcal{L}_4(U)_{2,i,j} &\approx (\nu((v_1)_{xx} + (v_1)_{yy}) + (\nu + \lambda)((v_1)_{xx} + (v_2)_{xy}))(x_{i,j}, t), \\
\mathcal{L}_4(U)_{3,i,j} &\approx (\nu((v_2)_{xx} + (v_2)_{yy}) + (\nu + \lambda)((v_1)_{xy} + (v_2)_{yy}))(x_{i,j}, t).
\end{aligned}$$

Here, as in the rest of this section, we drop the dependence of U on t to obtain the cited spatial semidiscretization.

The convective term \mathcal{C} is obtained through finite differences of numerical fluxes obtained by WENO5 reconstructions [2, 3] on Global Lax-Friedrichs flux splittings [15], which is fifth-order accurate for finite difference schemes, based on point values. Other schemes for systems of hyperbolic conservation laws could be used as well, see [17] and references therein.

To approximate the terms that involve derivatives of c in the conservation of momenta, we define finite difference operators for functions on $M \times M$ grids, for fixed $h > 0$, to approximate first-order derivatives:

$$\begin{aligned}
D_x^{1*} f_{i,j} &= \begin{cases} \frac{f_{i,j}}{h} & i = 1, \\ \frac{f_{i,j} - f_{i-1,j}}{h} & 1 < i < M, \\ \frac{-f_{i-1,j}}{h} & i = M. \end{cases} \\
D_x^1 f_{i,j} &= \begin{cases} \frac{f_{i+1,j} - f_{i,j}}{h} & i < M, \\ 0 & i = M. \end{cases} \\
D_x f_{i,j} &= \begin{cases} \frac{f_{i+1,j} - f_{i-1,j}}{2h} & 1 < i < M, \\ \frac{f_{i+1,j} - f_{i,j}}{h} & i = 1, \\ \frac{f_{i,j} - f_{i-1,j}}{h} & i = M. \end{cases} \\
D_x^* f_{i,j} &= \begin{cases} \frac{f_{i+1,j} - f_{i-1,j}}{2h} & 1 < i < M, \\ \frac{f_{i+1,j} - f_{i,j}}{2h} & i = 1, \\ \frac{f_{i,j} - f_{i-1,j}}{2h} & i = M. \end{cases} \\
S_x f_{i,j} &= \begin{cases} f_{i+1,j} & i < M, \\ 0 & i = M. \end{cases}
\end{aligned}$$

and likewise in the y direction.

1. $D_x^{1*} f_{i,j}$ is a second-order accurate approximation for $f_x(x_{i-\frac{1}{2}}, j)$ when $f_{i,j} = f(x_{i,j})$ and $f \in \mathcal{C}^3$ with $f(x_{0,j}) = f(x_{M,j}) = 0$, which is used to approximate pure double derivatives.

2. $D_x^1 f_{i,j}$ is a second-order accurate approximation for $f_x(x_{i+\frac{1}{2},j})$ when $f_{i,j} = f(x_{i,j})$ and $f \in \mathcal{C}^3$ with $f_x(x_{M+\frac{1}{2},j}) = 0$, which is used to approximate pure double derivatives. These two operators are related as $D_x^{1*} = -(D_x^1)^T$.
3. $D_x f_{i,j}$ is a second-order accurate approximation for $f_x(x_{i,j})$ for $1 < i, j < M$ and first-order accurate otherwise, when $f_{i,j} = f(x_{i,j})$ and $f \in \mathcal{C}^3$.
4. $D_x^* f_{i,j}$ is a second-order accurate approximation for $f_x(x_{i,j})$ for $1 < i, j < M$ or $j = 1, M$ and first-order accurate otherwise, when $f_{i,j} = f(x_{i,j})$ and $f \in \mathcal{C}^3$ with $f(x_{i,\frac{1}{2}}) = f(x_{i,M+\frac{1}{2}}) = 0$.

For the sake of notation, for functions f, g on $M \times M$ grids we denote $(f * g)_{i,j} = f_{i,j} g_{i,j}$.

We consider the following second-order accurate approximations at interior points $1 < i, j < M$ and first-order accurate at the rest of the points, for $c_{i,j} = \frac{(\rho c)_{i,j}}{\rho_{i,j}} \approx c(x_{i,j})$, in which the boundary conditions (3) on c are taken into account:

$$\begin{aligned}
(c_x^2)_x(x_{i,j}) &\approx (D_x^{1*}(D_x^1 C * D_x^1 C))_{i,j}, \\
(c_y^2)_x(x_{i,j}) &\approx (D_x((D_y^* C * D_y^* C)))_{i,j}, \\
(c_x c_y)_x(x_{i,j}) &\approx \frac{1}{2}(D_x^{1*}(D_x^1 C * (S_x D_y^* C + D_y^* C)))_{i,j}, \\
(c_y^2)_y(y_{i,j}) &\approx (D_y^{1*}(D_y^1 C * D_y^1 C))_{i,j}, \\
(c_x^2)_y(y_{i,j}) &\approx (D_y((D_x^* C * D_x^* C)))_{i,j}, \\
(c_y c_x)_y(y_{i,j}) &\approx \frac{1}{2}(D_y^{1*}(D_y^1 C * (S_y D_x^* C + D_x^* C)))_{i,j}
\end{aligned}$$

To approximate the terms that involve derivatives of v in the conservation of momenta, we consider the following finite difference approximation to $(v_k)_{xx}$, for $w = V_k, k = 1, 2,$, which is second-order accurate for $1 < i, j < M$ and first-order accurate otherwise under the no-slip boundary conditions on $v_k, k = 1, 2$

$$E_x w = \begin{cases} \frac{1}{h^2} \left(\frac{4}{3} w_{i+1,j} - 4 w_{i,j} \right) & i = 1, \\ \frac{1}{h^2} (w_{i+1,j} - 2 w_{i,j} + w_{i-1,j}) & 1 < i < M, \\ \frac{1}{h^2} (-4 w_{i,j} + \frac{4}{3} w_{i-1,j}) & i = M, \end{cases}$$

The E_y operator is defined analogously.

The approximations are:

$$\begin{aligned}
(v_k)_{xx}(x_{i,j}) &\approx (E_x V_k)_{i,j}, \\
(v_k)_{yy}(x_{i,j}) &\approx (E_y V_k)_{i,j}, \\
(v_k)_{xy}(x_{i,j}) &\approx (D_x(D_y V_k))_{i,j},
\end{aligned}$$

which lead to the $k = 2, 3$ M^2 blocks $\mathcal{L}_4^k(U)$ of $\mathcal{L}_4(U)$

$$\begin{bmatrix} \mathcal{L}_4^2(U), \\ \mathcal{L}_4^3(U) \end{bmatrix} = \begin{bmatrix} (2\nu + \lambda)I_M \otimes E + \nu E \otimes I_M & (\nu + \lambda)D \otimes D \\ (\nu + \lambda)D \otimes D & \nu I_M \otimes E + (2\nu + \lambda)E \otimes I_M \end{bmatrix} \begin{bmatrix} V_1 \\ V_2 \end{bmatrix},$$

where I_M is the $M \times M$ identity matrix, \otimes is the Kronecker product and

$$E = \frac{1}{h^2} \begin{bmatrix} -4 & \frac{4}{3} & 0 & \dots & 0 \\ 1 & -2 & 1 & \dots & 0 \\ \dots & \dots & \dots & \dots & \dots \\ 0 & \dots & 1 & -2 & 1 \\ 0 & \dots & 0 & \frac{4}{3} & -4 \end{bmatrix}, \quad D = \frac{1}{h} \begin{bmatrix} -1 & 1 & 0 & \dots & 0 \\ -\frac{1}{2} & 0 & \frac{1}{2} & \dots & 0 \\ \dots & \dots & \dots & \dots & \dots \\ 0 & \dots & -\frac{1}{2} & 0 & \frac{1}{2} \\ 0 & \dots & 0 & -1 & 1 \end{bmatrix}. \quad (10)$$

The matrices in (10) fail to be symmetric due to the boundary conditions. This could be circumvented with staggered grids for the velocity, but we do not consider this possibility in this paper.

The term $(\psi'(c))_{xx} = (\psi''(c)c_x)_x$ needs special care since it is not negatively definite due to $\psi''(c) = 3c^2 - 1$ changing sign in $(-1, 1)$. Following [18] we consider the splitting $\psi' = \phi_+ + \phi_-$

$$\begin{aligned} \phi_- &= c^3 - 3c, \phi_+ = 2c, \\ \phi'_-(c) &= 3(c^2 - 1) \leq 0, \phi'_+(c) = 2 > 0 \forall c \in [-1, 1]. \end{aligned}$$

For $\chi = \phi_{\pm}$, taking into account that $(\chi(c))_z = \chi'(c)c_z$, $z = x, y$, so $\chi(c)$ satisfies Neumann boundary conditions, we have the following second-order accurate approximations:

$$\begin{aligned} &(\chi(c))_{xx}(x_{i,j}) \\ &\approx \begin{cases} \frac{(\chi'(c_{i+1,j}) + \chi'(c_{i,j}))(c_{i+1,j} - c_{i,j})}{2h^2} & i = 1, \\ \frac{(\chi'(c_{i+1,j}) + \chi'(c_{i,j}))(c_{i+1,j} - c_{i,j}) - (\chi'(c_{i,j}) + \chi'(c_{i-1,j}))(c_{i,j} - c_{i-1,j})}{2h^2} & 1 < i < M, \\ \frac{-(\chi'(c_{i,j}) + \chi'(c_{i-1,j}))(c_{i,j} - c_{i-1,j})}{2h^2} & i = M. \end{cases} \\ &(\chi(c))_{yy}(x_{i,j}) \\ &\approx \begin{cases} \frac{(\chi'(c_{i,j+1}) + \chi'(c_{i,j}))(c_{i,j+1} - c_{i,j})}{2h^2} & j = 1, \\ \frac{(\chi'(c_{i,j+1}) + \chi'(c_{i,j}))(c_{i,j+1} - c_{i,j}) - (\chi'(c_{i,j}) + \chi'(c_{i,j-1}))(c_{i,j} - c_{i,j-1})}{2h^2} & 1 < j < M, \\ \frac{-(\chi'(c_{i,j}) + \chi'(c_{i,j-1}))(c_{i,j} - c_{i,j-1})}{2h^2} & j = M. \end{cases} \end{aligned} \quad (11)$$

These yield approximations

$$(\mathcal{M}_{\pm}(C)C)_{i,j} \approx \Delta(\phi_{\pm}(c))(x_{i,j}, t), \quad (12)$$

where we denote by $\mathcal{M}_{\pm}(C)$ the tensor built from the values of χ_{\pm} that appear in (11).

It can be seen that the boundary conditions $\nabla c(x, y, t) \cdot \mathbf{n}(x, y) = \nabla \mu(x, y, t) \cdot \mathbf{n}(x, y) = 0$ are equivalent to $\nabla c(x, y, t) \cdot \mathbf{n}(x, y) = \nabla \xi(x, y, t) \cdot \mathbf{n}(x, y) = 0$ for $\xi = \frac{1}{\rho} \Delta c$.

If $f(x, y)$ satisfies the Neumann boundary condition $\nabla f(x, y) \cdot \mathbf{n}(x, y) = 0$ and $f_{i,j} = f(x_{i,j})$ then $(\Delta_h f)_{i,j}$, $\Delta_h = \Delta_{x,h} + \Delta_{y,h}$, is a second-order accurate approx-

imation of $\Delta f(x_{i,j})$ for $f \in \mathcal{C}^4$, where

$$\Delta_{x,h} f_{i,j} = \begin{cases} \frac{f_{i+1,j} - f_{i,j}}{h^2} & i = 1, \\ \frac{f_{i+1,j} - 2f_{i,j} + f_{i-1,j}}{h^2} & 1 < i < M, \\ \frac{f_{i-1,j} - f_{i,j}}{h^2} & i = M. \end{cases}$$

$$\Delta_{y,h} f_{i,j} = \begin{cases} \frac{f_{i,j+1} - f_{i,j}}{h^2} & j = 1, \\ \frac{f_{i,j+1} - 2f_{i,j} + f_{i,j-1}}{h^2} & 1 < j < M, \\ \frac{f_{i,j-1} - f_{i,j}}{h^2} & j = M. \end{cases}$$

Therefore we get

$$\Delta \xi(x_{i,j}) \approx \left(\Delta_h (D(\varrho)^{-1} \Delta_h c) \right)_{i,j},$$

which, together with (12), yields the approximation

$$\Delta \mu(x_{i,j}) \approx \mathcal{L}_3^A(U)_{i,j} = \left(\mathcal{M}_+(C)C + \mathcal{M}_-(C)C - \varepsilon \Delta_h (D(\varrho)^{-1} \Delta_h C) \right)_{i,j}, \quad (13)$$

where $D(v), v \in \mathbb{R}^{M \times M}$, is the diagonal operator on $M \times M$ matrices given by

$$(D(v)w)_{i,j} = v_{i,j} w_{i,j}, i, j = 1, \dots, M.$$

The numerical schemes for the 1D case are obtained in a straightforward manner.

3.1 IMEX schemes

A Runge-Kutta solver, as the Explicit Euler method

$$U^{n+1} = U^n + \Delta t \mathcal{L}(U^n), \quad (14)$$

applied to obtain a fully discrete scheme would require $\Delta t \propto \Delta x^4$ for stability, which would yield a prohibitively expensive numerical scheme.

Instead, we use the technique of doubling variables and partitioned Runge-Kutta schemes [4, 13] to obtain Linearly IMPLICIT EXPLICIT schemes. We denote the variables that are to be treated explicitly with a tilde and define

$$\tilde{\mathcal{L}}(\tilde{U}, U) = \mathcal{C}(\tilde{U}) + \mathcal{L}_1(U) + \mathcal{L}_2(U) + \tilde{\mathcal{L}}_3(\tilde{U}, U) + \mathcal{L}_4(U),$$

where

$$\tilde{U} = \begin{bmatrix} \tilde{\varrho} \\ \tilde{\varrho} * \tilde{V}_1 \\ \tilde{\varrho} * \tilde{V}_2 \\ \tilde{\varrho} * \tilde{C} \end{bmatrix}, \quad U = \begin{bmatrix} \varrho \\ \varrho * V_1 \\ \varrho * V_2 \\ \varrho * C \end{bmatrix}, \quad \tilde{\mathcal{L}}_3(\tilde{U}, U) = \begin{bmatrix} 0 \\ 0 \\ 0 \\ \tilde{\mathcal{L}}_3^A(\tilde{U}, U) \end{bmatrix}$$

with

$$\tilde{\mathcal{L}}_3^A(\tilde{U}, U) = \mathcal{M}_+(\tilde{C})C + \mathcal{M}_-(\tilde{C})\tilde{C} - \varepsilon \Delta_h (D(\varrho)^{-1} \Delta_h C). \quad (15)$$

From (13) and (9), the requirement $\tilde{\mathcal{L}}(U, U) = \mathcal{L}(U)$ is met.

Now we have the IVP

$$\begin{aligned}\tilde{U}' &= \tilde{\mathcal{L}}(\tilde{U}, U) \\ U' &= \tilde{\mathcal{L}}(\tilde{U}, U) \\ \tilde{U}(0) &= U(0) = U_0\end{aligned}\tag{16}$$

is equivalent to

$$\begin{aligned}U' &= \mathcal{L}(U) \\ U(0) &= U_0.\end{aligned}$$

A partitioned Runge-Kutta scheme, in which there are two different s stages Butcher tableaus, one explicit and one (diagonally) implicit

$$\left. \begin{array}{c} \tilde{\gamma} \\ \hline \tilde{\beta}^T \end{array} \right| \tilde{\alpha}, \quad \tilde{\alpha}_{i,j} = 0, j \geq i \quad \left. \begin{array}{c} \gamma \\ \hline \beta^T \end{array} \right| \alpha, \quad \alpha_{i,j} = 0, j > i,$$

can be applied to (16). It can be seen that if both Butcher tableaus yield second-order accurate schemes and $\beta = \tilde{\beta}$, then the resulting partitioned Runge-Kutta scheme is second-order accurate.

This results in the recursion, for $i = 1, \dots, s$:

$$\begin{aligned}\tilde{U}^{(i)} &= \tilde{U}^n + \Delta t \sum_{j < i} \tilde{\alpha}_{i,j} \tilde{\mathcal{L}}(\tilde{U}^{(j)}, U^{(j)}), \\ U^{(i)} &= U^n + \Delta t \sum_{j < i} \alpha_{i,j} \tilde{\mathcal{L}}(\tilde{U}^{(j)}, U^{(j)}) + \Delta t \alpha_{i,i} \tilde{\mathcal{L}}(\tilde{U}^{(i)}, U^{(i)}), \\ \tilde{U}^{n+1} &= \tilde{U}^n + \Delta t \sum_{j=1}^s \tilde{\beta}_j \tilde{\mathcal{L}}(\tilde{U}^{(j)}, U^{(j)}), \\ U^{n+1} &= U^n + \Delta t \sum_{j=1}^s \beta_j \tilde{\mathcal{L}}(\tilde{U}^{(j)}, U^{(j)}) = \tilde{U}^{n+1},\end{aligned}$$

since $\tilde{\beta}_j = \beta_j, \forall j$ and $U^n = \tilde{U}^n$, and there is no need of doubling variables, which we henceforth assume.

The definitive recursion is the following:

$$\begin{aligned}\tilde{U}^{(i)} &= U^n + \Delta t \sum_{j < i} \tilde{\alpha}_{i,j} \mathcal{K}_j, \\ U^{(i)} &= U^n + \Delta t \sum_{j < i} \alpha_{i,j} \mathcal{K}_j + \Delta t \alpha_{i,i} \tilde{\mathcal{L}}(\tilde{U}^{(i)}, U^{(i)}), \\ U^{n+1} &= U^n + \Delta t \sum_{j=1}^s \beta_j \mathcal{K}_j,\end{aligned}$$

where

$$\mathcal{K}_j = \tilde{\mathcal{L}}(\tilde{U}^{(j)}, U^{(j)}).$$

We consider in this paper Stiffly Accurate Runge-Kutta solvers, i.e., the last row of the α matrix coincides with β^T . Specifically, we consider the following Butcher tableaux

$$\begin{array}{c} \text{EE-IE} \\ \begin{array}{c|c} 0 & 0 \\ \hline 1 & 1 \end{array} \end{array} \qquad \begin{array}{c} 1 \\ \hline 1 \end{array}$$

$$*\text{-DIRKSA} \begin{array}{c|cc} 0 & 0 & 0 \\ 1+s & 1+s & 0 \\ \hline & s & 1-s \end{array} \qquad \begin{array}{c|cc} 1-s & 1-s & 0 \\ 1 & s & 1-s \\ \hline & s & 1-s \end{array}, \quad s = \frac{1}{\sqrt{2}}.$$

The DIRKSA scheme is the only 2-stages second order stiffly accurate DIRK method with $\alpha_{ij} \geq 0$.

The order for EE-IE is 1 and it is 2 for *-DIRKSA.

3.2 Systems solutions

One needs to solve

$$U^{(i)} = U^n + \Delta t \sum_{j < i} \alpha_{i,j} \mathcal{K}_j + \Delta t \alpha_{i,i} \tilde{\mathcal{L}}(\tilde{U}^{(i)}, U^{(i)}), \quad (17)$$

for $U^{(i)}$, where

$$U^n = \begin{bmatrix} \varrho^n \\ M_1^n \\ M_2^n \\ Q^n \end{bmatrix}, \quad U^{(i)} = \begin{bmatrix} \varrho^{(i)} \\ M_1^{(i)} \\ M_2^{(i)} \\ Q^{(i)} \end{bmatrix} = \begin{bmatrix} \varrho^{(i)} \\ \varrho^{(i)} * V_1^{(i)} \\ \varrho^{(i)} * V_2^{(i)} \\ \varrho^{(i)} * C^{(i)} \end{bmatrix}.$$

As we shall see, although $\mathcal{L}_2, \tilde{\mathcal{L}}_3, \mathcal{L}_4$ are not linear, only linear systems for $V_k^{(i)}, C^{(i)}$ have to be solved.

For the first variable, with block superscript notation for the operators and \mathcal{K} variables, we get:

$$\varrho^{(i)} = \varrho^n + \Delta t \sum_{j < i} \alpha_{i,j} \mathcal{K}_j^1 + \Delta t \alpha_{i,i} \tilde{\mathcal{C}}^1(\tilde{U}^{(i)}),$$

so $\varrho^{(i)}$ is explicitly computable.

For the fourth variable $Q^{(i)}$, since $\varrho^{(i)}$ is already known, this system can be cast for the $C^{(i)}$ variables:

$$\begin{aligned} Q^{(i)} &= Q^n + \Delta t \sum_{j < i} \alpha_{i,j} \mathcal{K}_j^4 \\ &+ \Delta t \alpha_{i,i} \left(\tilde{\mathcal{C}}^4(\tilde{U}^{(i)}) + \mathcal{M}_+(\tilde{\mathcal{C}}^{(i)}) C^{(i)} + \mathcal{M}_-(\tilde{\mathcal{C}}^{(i)}) \tilde{\mathcal{C}}^{(i)} - \varepsilon \Delta_h D(\varrho^{(i)})^{-1} \Delta_h C^{(i)} \right), \end{aligned}$$

which is equivalent to

$$\begin{aligned} &\left(D(\varrho^{(i)}) - \Delta t \alpha_{i,i} \mathcal{M}_+(\tilde{\mathcal{C}}^{(i)}) + \Delta t \alpha_{i,i} \varepsilon \Delta_h D(\varrho^{(i)})^{-1} \Delta_h \right) C^{(i)} \\ &= Q^n + \Delta t \sum_{j < i} \alpha_{i,j} \mathcal{K}_j^4 + \Delta t \alpha_{i,i} \left(\tilde{\mathcal{C}}^4(\tilde{U}^{(i)}) + \mathcal{M}_-(\tilde{\mathcal{C}}^{(i)}) \tilde{\mathcal{C}}^{(i)} \right). \end{aligned} \quad (18)$$

If $\varrho_k^i > 0 \forall k$, then the matrix of this system is symmetric and positive definite, for is the sum of a diagonal positive matrix and two symmetric and positive semidefinite matrices.

For the second and third variables, one needs to solve:

$$\begin{aligned} \begin{bmatrix} \varrho^{(i)} * V_1^{(i)} \\ \varrho^{(i)} * V_2^{(i)} \end{bmatrix} &= \begin{bmatrix} M_1^n \\ M_2^n \end{bmatrix} + \Delta t \sum_{j < i} \alpha_{i,j} \begin{bmatrix} \mathcal{K}_j^2 \\ \mathcal{K}_j^3 \end{bmatrix} + \Delta t \alpha_{i,i} \begin{bmatrix} \mathcal{C}^2(\tilde{U}^{(i)}) + \mathcal{L}_1^2(U^{(i)}) + \mathcal{L}_2^2(U^{(i)}) \\ \mathcal{C}^3(\tilde{U}^{(i)}) + \mathcal{L}_1^3(U^{(i)}) + \mathcal{L}_2^3(U^{(i)}) \end{bmatrix} \\ + \Delta t \alpha_{i,i} &\begin{bmatrix} (2\nu + \lambda)I_M \otimes E + \nu E \otimes I_M & (\nu + \lambda)D \otimes D \\ (\nu + \lambda)D \otimes D & \nu I_M \otimes E + (2\nu + \lambda)E \otimes I_M \end{bmatrix} \begin{bmatrix} v_1^{(i)} \\ v_2^{(i)} \end{bmatrix}. \end{aligned}$$

Since $\mathcal{L}_1^j(U^{(i)})$ and $\mathcal{L}_2^j(U^{(i)})$, $j = 2, 3$, do not depend on $V_1^{(i)}, V_2^{(i)}$, they can be computed from previous steps and there only remains the following equation to be solved:

$$\begin{aligned} &\left(\begin{bmatrix} D(\varrho^{(i)}) & 0 \\ 0 & D(\varrho^{(i)}) \end{bmatrix} \right. \\ &- \Delta t \alpha_{i,i} \begin{bmatrix} (2\nu + \lambda)I_M \otimes E + \nu E \otimes I_M & (\nu + \lambda)D \otimes D \\ (\nu + \lambda)D \otimes D & \nu I_M \otimes E + (2\nu + \lambda)E \otimes I_M \end{bmatrix} \left. \right) \begin{bmatrix} V_1^{(i)} \\ V_2^{(i)} \end{bmatrix} \quad (19) \\ &= \begin{bmatrix} M_1^n \\ M_2^n \end{bmatrix} + \Delta t \sum_{j < i} \alpha_{i,j} \begin{bmatrix} \mathcal{K}_j^2 \\ \mathcal{K}_j^3 \end{bmatrix} + \Delta t \alpha_{i,i} \begin{bmatrix} \mathcal{C}^2(\tilde{U}^{(i)}) + \mathcal{L}_1^2(U^{(i)}) + \mathcal{L}_2^2(U^{(i)}) \\ \mathcal{C}^3(\tilde{U}^{(i)}) + \mathcal{L}_1^3(U^{(i)}) + \mathcal{L}_2^3(U^{(i)}) \end{bmatrix}. \end{aligned}$$

If $\varrho_k^i > 0 \forall k$, then the matrix of this system should be close to symmetric and positive definite, since the matrix

$$- \begin{bmatrix} (2\nu + \lambda)I_M \otimes E + \nu E \otimes I_M & (\nu + \lambda)D \otimes D \\ (\nu + \lambda)D \otimes D & \nu I_M \otimes E + (2\nu + \lambda)E \otimes I_M \end{bmatrix}$$

is a discretization of the self-adjoint elliptic operator

$$- \left((\nu + \lambda) \nabla \operatorname{div} \mathbf{v} + \nu \Delta \mathbf{v} \right),$$

under the boundary conditions (3).

3.3 Linear solvers

We have used the multigrid V-cycle algorithm with 4 pre- and post- Gauss-Seidel smoothings and direct solution when the size of the projected systems is ≤ 4 (see [5]) for the solution of systems (18) and (19).

The matrix in system (18) is symmetric and positive, so there is the possibility of using the conjugate gradient method, using the following approximation

$$\begin{aligned} A &= D(\varrho^{(i)}) - \Delta t \alpha_{i,i} \mathcal{M}_+(\tilde{C}^{(i)}) + \Delta t \alpha_{i,i} \varepsilon \Delta_h D(\varrho^{(i)})^{-1} \Delta_h \\ &\approx B = \mu_1 I_{M^2} + \Delta t \alpha_{i,i} \mu_2 \Delta_h + \Delta t \alpha_{i,i} \varepsilon \mu_3 \Delta_h^2, \\ \mu_1 &= \operatorname{mean}(\varrho^{(i)}), \quad \mu_2 = \operatorname{mean}(\phi'_+(\tilde{C}^{(i)})) = 2, \quad \mu_3 = \operatorname{mean}(1/\varrho^{(i)}), \end{aligned}$$

as preconditioner, for Δ_h can be efficiently diagonalized by discrete cosine transforms.

We next analyze the condition number of the preconditioned matrix:

$$\frac{\max_{z \neq 0} \frac{z^T A z}{z^T B z}}{\min_{z \neq 0} \frac{z^T A z}{z^T B z}}.$$

We drop the superindex ⁽ⁱ⁾ for simplicity. The matrix $\mathcal{M}_+(\tilde{C})$ can be expressed as

$$\begin{aligned} \mathcal{M}_+(\tilde{C}) &= -(I_M \otimes D_1^T)D(\lambda^x)(I_M \otimes D_1) - (D_1^T \otimes I_M)D(\lambda^y)(D_1 \otimes I_M) \\ D_1 &= \frac{1}{h} \begin{bmatrix} -1 & 1 & 0 & \dots & 0 \\ 0 & -1 & 1 & \dots & 0 \\ \dots & \dots & \dots & \dots & \dots \\ 0 & \dots & 0 & -1 & 1 \\ 0 & \dots & 0 & 0 & 0 \end{bmatrix} \in \mathbb{R}^{M \times M}, \\ \lambda_{i+M(j-1)}^x &= \begin{cases} \frac{1}{2}(\phi'_+(C_{i+M(j-1)}) + \phi'_+(C_{i+1+M(j-1)})) & i < M \\ 0 & i = M \end{cases} \\ \lambda_{i+M(j-1)}^y &= \begin{cases} \frac{1}{2}(\phi'_+(C_{i+M(j-1)}) + \phi'_+(C_{i+M(j)})) & j < M \\ 0 & j = M; \end{cases} \end{aligned}$$

Since $\phi'_+ = 2$ and

$$-(I_M \otimes D_1^T)(I_M \otimes D_1) - (D_1^T \otimes I_M)(D_1 \otimes I_M) = \Delta_h,$$

we get the following:

$$\begin{aligned} z^T A z &= \sum_{k=1}^{M^2} \varrho_k z_k^2 + 2\Delta t \alpha_{i,i} \left(\sum_{k=1}^{M^2} ((I_M \otimes D_1)z)_k^2 + ((D_1 \otimes I_M)z)_k^2 \right) \\ &\quad + \Delta t \alpha_{i,i} \varepsilon \Delta_h \sum_{k=1}^{M^2} \frac{1}{\varrho_k} (\Delta_h z)_k^2 \\ z^T B z &= \mu_1 \sum_{k=1}^{M^2} z_k^2 + 2\Delta t \alpha_{i,i} \left(\sum_{k=1}^{M^2} ((I_M \otimes D_1)z)_k^2 + ((D_1 \otimes I_M)z)_k^2 \right) \\ &\quad + \mu_3 \Delta t \alpha_{i,i} \varepsilon \Delta_h \sum_{k=1}^{M^2} (\Delta_h z)_k^2. \end{aligned}$$

Therefore, for $0 \neq z \in \mathbb{R}^{M^2}$:

$$\min \left(\frac{\min \varrho_j}{\mu_1}, \frac{\min \frac{1}{\varrho_j}}{\mu_3} \right) \leq \frac{z^T A z}{z^T B z} \leq \max \left(\frac{\max \varrho_j}{\mu_1}, \frac{\max \frac{1}{\varrho_j}}{\mu_3} \right)$$

therefore the condition of the preconditioned matrix is bounded above by

$$\frac{\max \left(\frac{\max \varrho_j}{\mu_1}, \frac{\max \frac{1}{\varrho_j}}{\mu_3} \right)}{\min \left(\frac{\min \varrho_j}{\mu_1}, \frac{\min \frac{1}{\varrho_j}}{\mu_3} \right)},$$

which is close to 1 if ϱ is nearly constant. Therefore, it is expected to be a good preconditioner in this case.

3.4 Time-step selection

The time-step stability restrictions of the purely convective subsystem is

$$\Delta t = \text{CFL} \cdot \text{cs} \cdot \Delta x, \quad (20)$$

where CFL is a constant and the maximum of the characteristic speeds, cs, is computed, at each Runge-Kutta step, as

$$\text{cs} = \max_{k=1,2,j=1,\dots,M^2} |V_{k,j}^{(i)}| + \sqrt{\gamma(\varrho_j^{(i)})^{\gamma-1}}.$$

The scheme is not ensured to be bound preserving, i.e., it might happen that density might become negative or the c -variable be outside $[-1, 1]$. Purely convective models might develop vacuum regions and coping with this possibility is certainly challenging.

In our case, there is no guarantee that the solution of (18) be in $[-1, 1]$. We have used in our simulation the strategy of decreasing Δt when $|c|$ reaches some threshold (1.5 in the experiments) and increasing it until the maximum otherwise.

4 Numerical experiments

The objectives of the experiments in this section are the following:

1. Showing that the order of the global errors in some experiments coincides with the expected design order of the scheme used to obtain them.
2. Showing that some IMEX schemes can perform time steps Δt with the same stability restrictions as the purely convective subsystem, see (20).
3. Testing the behavior of different issues for the algorithms, such as conservation, number of iterations for the linear solvers, etc.

In all numerical experiments, the adiabatic constant γ has been set to 5/3.

All the results have been obtained with a C++ implementation, using the GNU C++ compiler with optimizations -O3 and running in a single core of an AMD EPYC 7282 3.0 GHz CPU. The matrices of systems (18) and (19) are stored by diagonals.

4.1 Stability test

We consider the following initial condition for a one-dimensional test: (c_0 in unstable region $(-\frac{1}{\sqrt{3}}, \frac{1}{\sqrt{3}})$)

$$\begin{aligned} \rho_0(x) &= 0.1 \cos(2\pi x) + 1.25 \\ v_0(x) &= \sin(\pi x) \\ c_0(x) &= 0.1 \cos(\pi x) \end{aligned}$$

with parameters $G = -10$, $\nu_* = 2\nu + \lambda = 2$, $\varepsilon = 10^{-4}$. The Explicit Euler scheme (14) blows up for $M = 8000$, and $\Delta t = \Delta x^3$ for $t \approx 6 \cdot 10^{-11}$, thus indicating that Δt should be proportional to Δx^4 for stable simulations.

The EE-IE and *-DIRKSA blow up for $M = 100$ and Δt computed by (20) for CFL = 1.1 for $t \approx 10^{-1}$, whereas they do not for CFL = 1 and $M = 10000$.

4.2 Order test

This test aims to the assessment that the *-DIRKSA method achieves second-order accuracy in the global errors. For this purpose, we add a forcing term to the equations so that the solution is prescribed. Specifically, the solution in this case is

$$\begin{aligned}\rho(x, y, t) &= \frac{\cos(2\pi x) \cos(\pi y) (t+1)}{10} + \frac{5}{4}, \\ v_1(x, y, t) &= -\sin(\pi x) \sin(\pi y) (2t^2 - 1), \\ v_2(x, y, t) &= \sin(\pi x) \sin(2\pi y) (t^2 + 1), \\ c(x, y, t) &= \frac{3}{4} - \frac{\cos(\pi x) \cos(\pi y) (t-1)}{10}.\end{aligned}$$

Notice that these functions satisfy the boundary conditions (3).

The parameters that have been used are the following:

$$\nu = 1, \quad \lambda = 10^{-1}, \quad \varepsilon = 10^{-4}, \quad G = -10.$$

For these tests, we have used Δt given by (20) with CFL=0.4.

For $M \times M$ grids, with $M = 2^l$, $l = 3, \dots, 8$, the global errors for the approximations $u_{k,i,j}^n$ obtained by the *-DIRKSA method for $t_n = T = 0.01$, are computed as

$$e_M = \frac{1}{M^2} \sum_{k=1}^4 \sum_{i,j=1}^M |u_{k,i,j}^n - u_k(x_{i,j}, T)|,$$

and are displayed in Table 1, where it can be observed the convergence of the quotients e_M/e_{2M} towards 4. The analogous experiment is performed for the EE-EI scheme resulting in quotients e_M/e_{2M} that decrease away from 4.

*-DIRKSA			EE-EI		
M	e_M	e_M/e_{2M}	M	e_M	e_M/e_{2M}
8	1.9828e-02	4.62	8	1.4989e-02	4.76
16	4.2964e-03	4.12	16	3.1522e-03	3.38
32	1.0422e-03	3.92	32	9.3289e-04	3.40
64	2.6617e-04	3.93	64	2.7460e-04	3.31
128	6.7802e-05	3.95	128	8.2857e-05	3.02
256	1.7148e-05	—	256	2.7457e-05	—

Table 1 Computed orders of convergence of global errors of *-DIRKSA and EE-EI IMEX schemes for the test with a forced solution.

4.3 Two-dimensional tests.

For the following two-dimensional tests we have used Δt given by (20) with CFL=0.4, which is a safe setup for simulations with the corresponding explicit schemes for the convective part only (isentropic Euler equations).

We consider the following tests:

- Test 1 (c_0 in unstable region $(-\frac{1}{\sqrt{3}}, \frac{1}{\sqrt{3}})$):

$$\begin{aligned}\rho_0(x, y) &= 0.1 \cos(2\pi x) \cos(\pi y) + 1.25 \\ \mathbf{v}_0(x, y) &= (\sin(\pi x) \sin(\pi y), \sin(\pi x) \sin(2\pi y)) \\ c_0(x, y) &= 0.1 \cos(\pi x) \cos(\pi y)\end{aligned}$$

- Test 2 (c_0 in stable region):

$$\begin{aligned}\rho_0(x, y) &= 0.1 \cos(2\pi x) \cos(\pi y) + 1.25 \\ \mathbf{v}_0(x, y) &= (\sin(\pi x) \sin(\pi y), \sin(\pi x) \sin(2\pi y)) \\ c_0(x, y) &= 0.75 + 0.1 \cos(\pi x) \cos(\pi y)\end{aligned}$$

- Test 3: $\rho = 1$, $\mathbf{v}_0 = 0$, c_0 uniform random sample of 0 mean and 10^{-10} standard deviation.

Notice that these functions satisfy the boundary conditions (3) (for test 3, almost within roundoff error).

In Figure 1, we show the time evolution of the conservation errors for ρ and $q = \rho c$ for Test 3, and parameters $\nu = 10^{-3}$, $\lambda = 10^{-4}$, $\nu = 10^{-4}$, $M = 256$, with multigrid with relative decrease of residual of 10^{-12} as stopping criterion. Specifically, we approximate

$$\begin{aligned}\int_{\Omega} \rho(x, t_n) dx - \int_{\Omega} \rho(x, 0) dx &\approx \text{err}_{\rho}(t_n) = \sum_{i,j=1}^M \varrho_{i,j}^n - \sum_{i,j=1}^M \varrho_{i,j}^0 \\ \int_{\Omega} \rho(x, t_n) dx - \int_{\Omega} \rho(x, 0) dx &\approx \text{err}_q(t_n) = \sum_{i,j=1}^M Q_{i,j}^n - \sum_{i,j=1}^M Q_{i,j}^0\end{aligned}$$

In Figure 2 we show the time evolution of the CFL parameter, according to subsection 3.4, for a specially challenging case for Test 1, with parameters $\nu = 10^{-3}$, $\lambda = 10^{-4}$, $\varepsilon = 10^{-5}$, $M = 256$.

We show in Figures 3-11 some snapshots of the results obtained for all the tests with *-DIRKSA, $M = 256$, $G = -10$, $\nu = 10^{-3}$, $\lambda = 10^{-4}$, $\varepsilon = 10^{-4}$, which correspond to flows with Reynolds number roughly in the range $[10^2, 10^3]$.

In Figure 3, it can be seen that the c -component in the initial condition for Test 1 lies entirely within the spinodal region $(-\frac{1}{\sqrt{3}}, \frac{1}{\sqrt{3}})$. Therefore, at the early stages of the simulation, at $T = 0.1$, separation occurs forming complex patterns. Meanwhile, it can be appreciated from the pictures corresponding to the ρ -variable that gravity is acting so that density increases at the bottom boundary, $y = 0$. This trend continues in Figure 4, where it can be appreciated that the maximal density continues increasing, a sharp upgoing front develops for all the variables, but c , where the diffuse interface experiments many topological changes, with growing

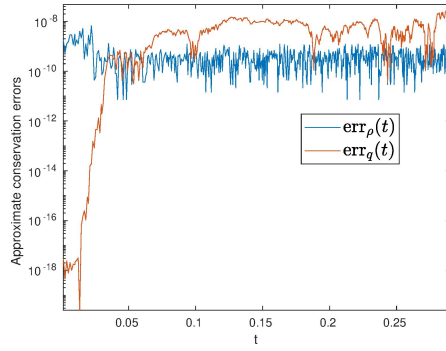


Fig. 1 Conservation errors for test 3.

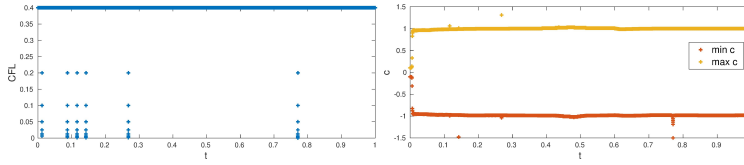


Fig. 2 Test 1. Left: Time evolution of the CFL parameter; Right: Time evolution of $\min c$, $\max c$.

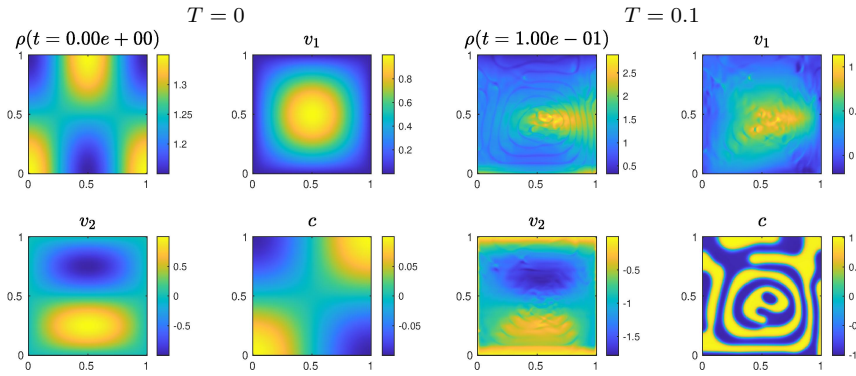


Fig. 3 Results for Test 1. Left: Initial condition, with c -variable inside spinodal region; Right: Results for $T = 0.1$, where density increases at the bottom and separation is clearly visible in the c -variable.

regions, a phenomenon named nucleation. At the final stages of the simulation, as seen in Figure 5, the maximal density decreases, nucleation continues and the bulk flow enters into a seemingly turbulent regime.

In Figure 6, it can be seen that the c -component in the initial condition for Test 2 lies above the spinodal region. Therefore, as seen in the pictures for the c -variable in the snapshots shown in this Figure and also in Figure 7, the fluid remains almost homogeneous, with c tending to $3/4$ in the whole domain, which corresponds to mass fractions $c_1 = \frac{7}{8}, c_2 = \frac{1}{8}$, which are exactly the initial pro-

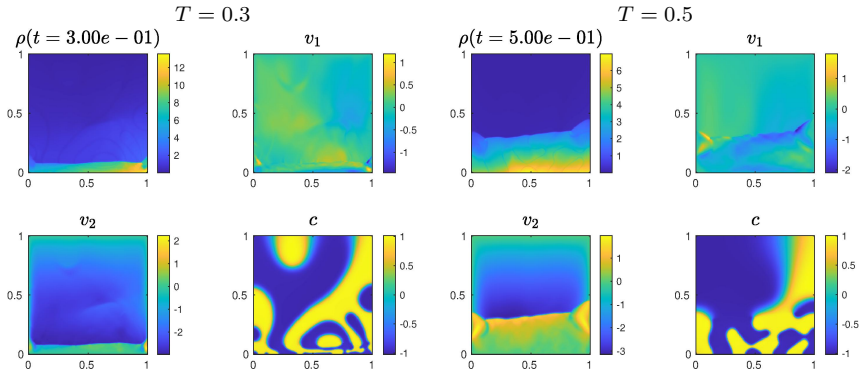


Fig. 4 Results for Test 1, $T = 0.3$ (left) and $T = 0.5$ (right) where it can be seen that density continues increasing at the bottom, forming an upgoing front, and nucleation is beginning, as seen in the c -variable.

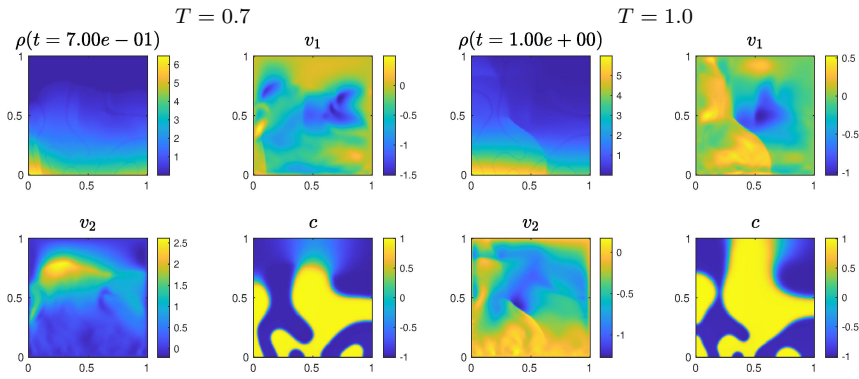


Fig. 5 Results for Test 1, $T = 0.7$ (left) and $T = 1.0$ (right) where it can be seen in the velocity that vorticity has developed and nucleation is increasing, as seen in the c -variable.

portions of the individual species. This fact means that the rest of the equations behave like a uniform fluid governed by the compressible Navier-Stokes equations under gravitation, with Reynolds number high enough for a seemingly turbulent regime.

In Figure 8, it can be seen that the c -component in the initial condition for Test 3 is almost 0, thus lies entirely within the spinodal region $(-\frac{1}{\sqrt{3}}, \frac{1}{\sqrt{3}})$. Therefore, at the early stages of the simulation, at $T = 0.01$, a typical spinodal decomposition begins appearing in the form of a medium-frequency pattern, corresponding to a solution as in (7)-(8), for $k_1, k_2 \in \mathbb{N}$ that minimize

$$-(k_1^2 + k_2^2) + \varepsilon \pi^2 (k_1^2 + k_2^2)^2,$$

corresponding to the expression in (8), for $c_0 = 0$, taking into account that $\psi''(c_0) = -1$.

The rest of the simulation can be seen in Figures 9-11, where the spinodal decomposition continues until nucleation. Density increases at the bottom, but no

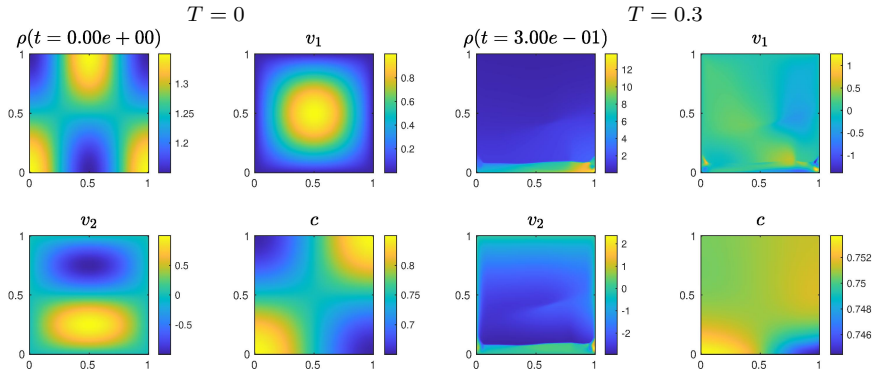


Fig. 6 Results for Test 2. Left: Initial condition, with c -variable above the spinodal region; Right: Results for $T = 0.3$, where it can be seen that density continues increasing at the bottom, forming an upgoing front, while the c -variable is converging towards 0.75.

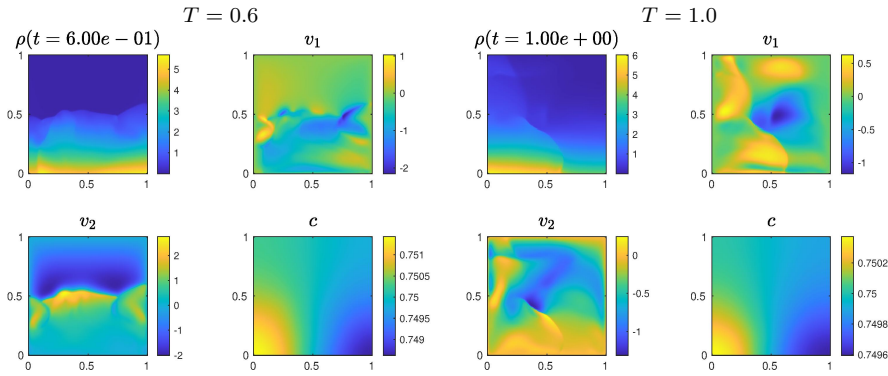


Fig. 7 Results for Test 2, $T = 0.6$ (left) and $T = 1.0$ (right) where it can be seen in the velocity that vorticity has developed, while the c -variable has almost fully converged to 0.75.

clear turbulence is appreciated, maybe due to the simulation having been carried only until $T = 0.29$.

4.4 Linear solvers

The multigrid solver mentioned in subsection 3.3 for the solution of (19) has shown a very satisfactory performance throughout all tests, requiring almost always only one iteration to achieve convergence to double precision digits.

The performance of the solvers for the solution of (18) is more complex. In tables 2, 3 and 4 we show the average number of multigrid iterations to solve (18) for tests 1, 2, 3, respectively, with $\nu = 10^{-2}, 10^{-3}, 10^{-4}$ and $\varepsilon = 10^{-3}, 10^{-4}, 10^{-5}$, for a stopping criterion based on a relative decrease of the residual by a factor of 10^{-6} .

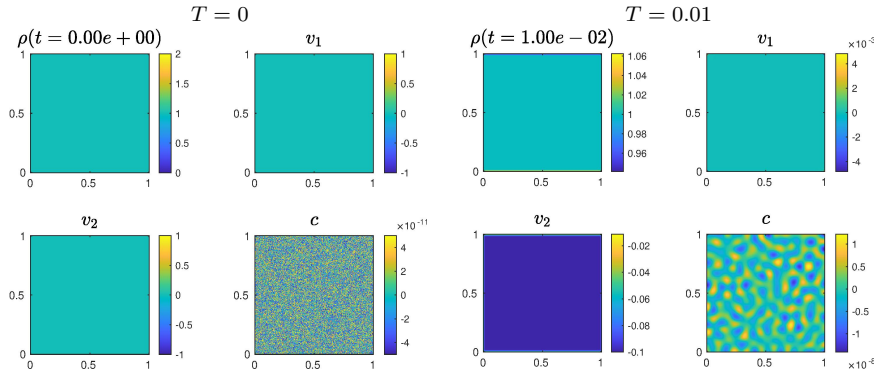


Fig. 8 Test 3. Left: Initial condition, where it can be seen that the c -component is in the range $(-5 \cdot 10^{-11}, 1 \cdot 10^{-11})$, thus lies entirely within the spinodal region $(-\frac{1}{\sqrt{3}}, \frac{1}{\sqrt{3}})$; Right: for $T = 0.01$ onset of a spinodal decomposition begins appearing with an amplitude around 10^{-8} .

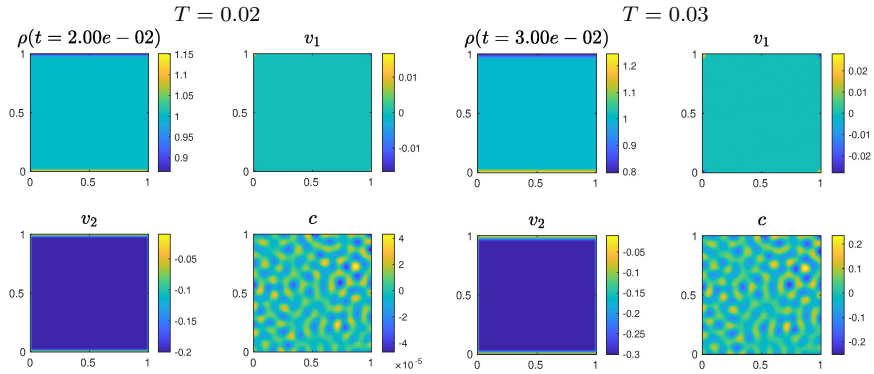


Fig. 9 Results for Test 3, where it can be seen that density increases at the bottom and the spinodal decomposition continues its development with an amplitude around $4 \cdot 10^{-5}$ for $T = 0.02$ (left) and 0.2 for $T = 0.03$ (right).

It can be deduced from these tables that the number of iterations grows slowly with M for all cases.

In Table 5 we show a comparison between the multigrid and the preconditioned conjugate gradient solvers in subsection 3.3. The results have been obtained with *-DIRKSA, $M = 16, 32, 64, 128, 256$, $G = -10$, $\nu = 10^{-2}$, $\lambda = 10^{-3}$, $\varepsilon = 10^{-4}$. It can be deduced that the preconditioned conjugate gradient solver uses less CPU time than the multigrid solver, although the latter takes fewer iterations than the former.

5 Conclusions and future work

In this paper, we propose efficient linearly implicit-explicit schemes for the two-dimensional compressible isentropic Cahn-Hilliard-Navier-Stokes equations. Some

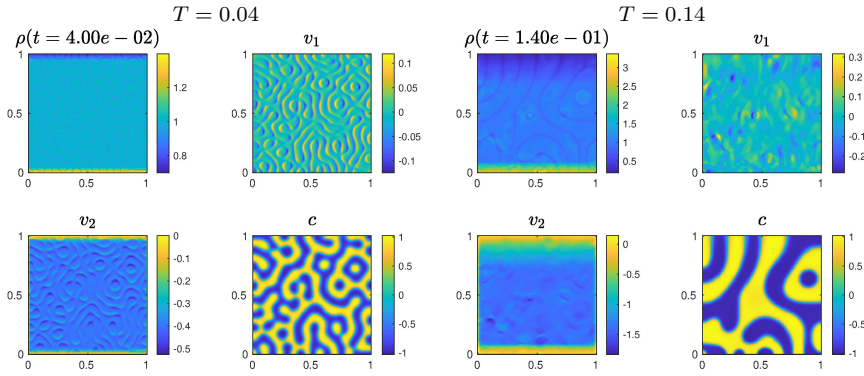


Fig. 10 Results for Test 3, where it can be seen that density continues increasing at the bottom and the spinodal decomposition has given a fully developed separation pattern for $T = 0.04$ (left), which has continued towards the onset of nucleation for $T = 0.14$ (right).

M/ν	$\varepsilon = 10^{-3}$			$\varepsilon = 10^{-4}$			$\varepsilon = 10^{-5}$		
	10^{-1}	10^{-2}	10^{-3}	10^{-1}	10^{-2}	10^{-3}	10^{-1}	10^{-2}	10^{-3}
16	2.4	2.8	3.3	1.9	2.5	3.1	1.8	1.9	2.1
32	3.5	4.1	5.8	2.3	3.2	3.8	2.0	2.0	2.7
64	4.2	5.2	4.5	3.6	3.8	4.2	2.2	2.3	3.0
128	5.1	6.4	5.6	4.4	4.5	5.7	3.1	3.7	3.8
256	5.9	7.3	6.3	4.8	5.6	6.8	3.8	3.9	4.5

Table 2 Average number of multigrid iterations to solve (18) for Test 1.

M/ν	$\varepsilon = 10^{-3}$			$\varepsilon = 10^{-4}$			$\varepsilon = 10^{-5}$		
	10^{-1}	10^{-2}	10^{-3}	10^{-1}	10^{-2}	10^{-3}	10^{-1}	10^{-2}	10^{-3}
16	1.2	1.2	1.3	1.1	1.1	1.2	1.1	1.1	1.1
32	1.3	1.3	1.6	1.1	1.1	1.3	1.1	1.1	1.2
64	1.4	1.6	2.2	1.1	1.2	1.3	1.1	1.3	1.4
128	1.6	1.9	2.9	1.2	1.2	1.2	1.2	1.4	1.4
256	1.8	2.3	3.4	1.3	1.3	1.3	1.3	1.4	1.4

Table 3 Average number of multigrid iterations to solve (18) for Test 2.

tests are performed to show that they achieve second-order accuracy under time-step stability restrictions dictated only by the convective part of the equations.

As future research, we plan to extend these techniques to other, stiffer pressure laws, and to a three-dimensional setting with Galerkin techniques. We also plan the extension of these techniques to quasi-incompressible models (see [12]).

A crucial part of the algorithms is the iterative linear solvers used for solving the system related to the Cahn-Hilliard subequation. We plan to explore the possibility of using the multigrid solver as preconditioner for the conjugate gradient solver.

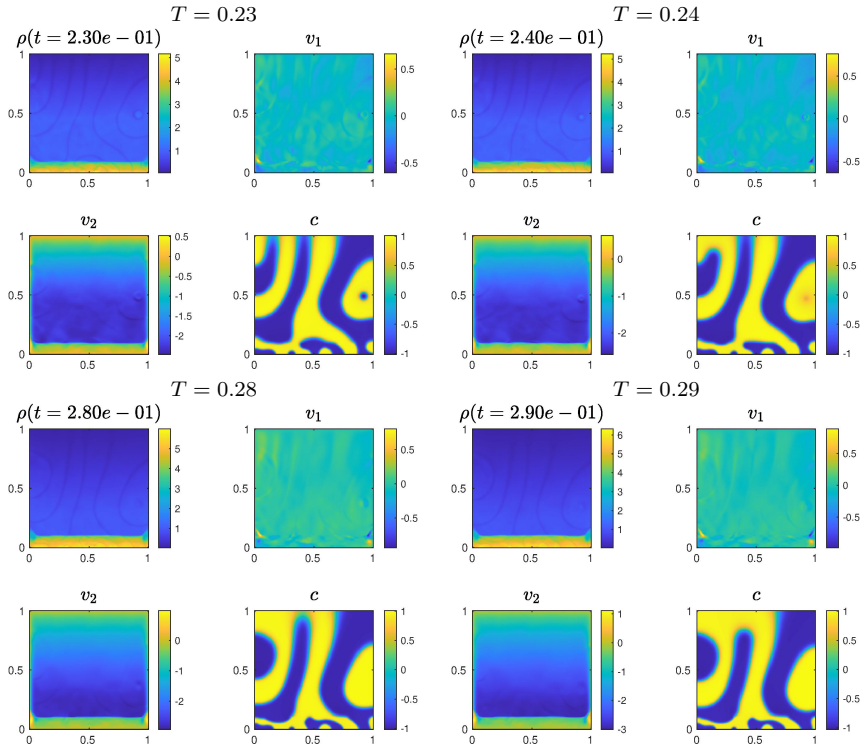


Fig. 11 Results for Test 3, where nucleation is visible in the c -variable near $(0.9, 0.5)$, with an ever-shrinking region of the second fluid disappearing.

M/ν	$\varepsilon = 10^{-3}$			$\varepsilon = 10^{-4}$			$\varepsilon = 10^{-5}$		
	10^{-1}	10^{-2}	10^{-3}	10^{-1}	10^{-2}	10^{-3}	10^{-1}	10^{-2}	10^{-3}
16	3.3	3.1	3.1	2.6	2.3	2.4	2.6	2.3	2.3
32	4.5	4.4	4.5	3.3	2.9	3.0	3.1	2.7	2.8
64	6.4	5.6	5.5	4.5	3.7	3.7	4.3	3.8	3.4
128	6.5	6.0	5.5	6.4	5.7	5.3	5.4	4.4	4.0
256	7.0	6.0	5.5	7.0	6.0	5.5	7.2	5.7	5.4

Table 4 Average number of multigrid iterations to solve (18) for Test 3.

Acknowledgments

I wish to express my gratitude to Raimund Bürger, from the University of Concepción, Chile, for suggesting to look at Siano's paper [16] and to Rafael Ordóñez for preliminary work on Cahn-Hilliard simulations.

This paper has received financial support from the research projects PID2020-117211GB-I00, granted by MCIN/ AEI /10.13039/501100011033, and CIAICO/2021/227, granted by GVA.

	CG		MG	
M	avg. its.	CPU	avg. its.	CPU
16	10.00	0.05	2.96	0.07
32	10.48	0.30	3.00	0.40
64	12.27	2.22	3.20	2.53
128	15.61	15.46	4.54	19.53
256	18.05	137.27	5.96	195.80

Table 5 Comparison of average number of iterations and CPU time for the preconditioned conjugate gradient and multigrid solvers for (18) and Test 1.

References

1. Helmut Abels and Eduard Feireisl. On a diffuse interface model for a two-phase flow of compressible viscous fluids. *Indiana Univ. Math. J.*, 57(2):659–698, 2008.
2. Antonio Baeza, Raimund Burger, Pep Mulet, and David Zorio. On the Efficient Computation of Smoothness Indicators for a Class of WENO Reconstructions. *Journal of Scientific Computing*, 80(2):1240–1263, AUG 2019.
3. Antonio Baeza, Raimund Burger, Pep Mulet, and David Zorio. WENO Reconstructions of Unconditionally Optimal High Order. *SIAM Journal on Numerical Analysis*, 57(6):2760–2784, 2019.
4. Sebastiano Boscarino, Raimund Bürger, Pep Mulet, Giovanni Russo, and Luis M. Villada. Linearly Implicit Imex Runge-Kutta Methods for a Class of Degenerate Convection-Diffusion Problems. *SIAM J. Sci. Comp.*, 37(2):B305–B331, 2015.
5. Achi Brandt and Oren E. Livne. *Multigrid techniques—1984 guide with applications to fluid dynamics*, volume 67 of *Classics in Applied Mathematics*. Society for Industrial and Applied Mathematics (SIAM), Philadelphia, PA, revised edition, 2011.
6. J.W. Cahn and J.E. Hilliard. Free energy of a nonuniform system .3. Nucleation in a 2-component incompressible fluid. *J. Chem. Phys.*, 31(3):688–699, 1959.
7. C. M. Elliott. The Cahn-Hilliard model for the kinetics of phase separation. In *Mathematical models for phase change problems (Óbidos, 1988)*, volume 88 of *Internat. Ser. Numer. Math.*, pages 35–73. Birkhäuser, Basel, 1989.
8. Charles M. Elliott and Donald A. French. Numerical Studies of the Cahn-Hilliard Equation for Phase Separation. *IMA Journal of Applied Mathematics*, 38(2):97–128, 05 1987.
9. Qiaolin He and Xiaoding Shi. Numerical Study of Compressible Navier-Stokes-Cahn-Hilliard System. *Comm. Math. Sci.*, 18(2):571–591, 2020.
10. D. Jacqmin. Calculation of two-phase Navier-Stokes flows using phase-field modeling. *Journal of Computational Physics*, 155(1):96–127, OCT 10 1999.
11. GJ Kynch. A Theory of Sedimentation. *Trans. Faraday Soc.*, 48(2):166–176, 1952.
12. J. Lowengrub and L. Truskinovsky. Quasi-incompressible Cahn-Hilliard fluids and topological transitions. *Proc. Royal Soc. A*, 454(1978):2617–2654, 1998.
13. L. Pareschi and G. Russo. Implicit-explicit Runge-Kutta schemes and applications to hyperbolic systems with relaxation. *J. Sci. Comput.*, 25(1/2):129–155, 2005.
14. Jie Shen and Xiaofeng Yang. Numerical Approximations of Allen-Cahn and Cahn-Hilliard Equations. *Discrete and Continuous Dynamical Systems*, 28(4):1669–1691, DEC 2010.
15. Chi-Wang Shu. High Order Weighted Essentially Nonoscillatory Schemes for Convection Dominated Problems. *SIAM Rev.*, 51(1):82–126, 2009.
16. Donald B. Siano. Layered sedimentation in suspensions of monodisperse spherical colloidal particles. *J. Colloid and Interface Sci.*, 68(1):111–127, 1979.
17. E. F. Toro. *Riemann solvers and numerical methods for fluid dynamics*. Springer, third edition edition, 2009.
18. BP Vollmayr-Lee and AD Rutenberg. Fast and accurate coarsening simulation with an unconditionally stable time step. *Phys. Rev. E*, 68(6, 2), 2003.
19. PT Yue, JJ Feng, C Liu, and J Shen. A diffuse-interface method for simulating two-phase flows of complex fluids. *Journal of Fluid Mechanics*, 515:293–317, SEP 25 2004.